RSC Advances

PAPER

View Article Online
View Journal | View Issue



Cite this: *RSC Adv.*, 2023, **13**, 24450

# A novel cobalt(II) acetate complex bearing lutidine ligand: a promising electrocatalyst for oxygen evolution reaction†

Deepika Tanwar,‡[ab] Priya Jain,‡[c] Deepali Ahluwalia,[d] Athul Sudheendranath,[c] Sajesh P. Thomas,[c] Pravin P. Ingole *[c] and Umesh Kumar *[a]

Developing cost-effective electrocatalysts using earth-abundant metal as an alternative to expensive precious metal catalyst remains a key challenge for researchers. Several strategies are being researched/tested for making low-cost transition metal complexes with controlled electron-density and coordination flexibility around the metal center to enhance their catalytic activity. Herein, we report a novel lutidine coordinated cobalt(II) acetate complex $[(3,5\text{-lutidine})_2Co(OAc)_2(H_2O)_2]$ (**1**) as a promising electrocatalyst for oxygen evolution reaction (OER). Complex **1** was characterized by FT-IR, elemental analysis, and single crystal X-ray diffraction data. The structure optimization of complex **1** was also done using DFT calculation and the obtained geometrical parameters were found to be in good agreement with the parameters obtained from the solid state structure obtained through single crystal X-ray diffraction data. Further, the molecular electrostatic potential (MEP) maps analysis of complex **1** observed electron rich centers that were found to be in agreement with the solid-state structure. It was understood that the coordination of lutidine as a Lewis base and acetate moiety as a flexible ligand will provide more coordination flexibility around the metal center to facilitate the catalytic reaction. Further, the electron rich centers around metal center will also support the enhancement of their catalytic activity. Complex **1** shows impressive OER activity, even better than the state-of-the-art $IrO_2$ catalyst, in terms of turnover frequency (TOF: 0.05) and onset potential (1.50 V *vs.* RHE). The TOF for complex **1** is two and half times higher, while the onset potential is *ca.* 20 mV lower, than the benchmark $IrO_2$ catalyst studied under identical conditions.

Received 13th July 2023
Accepted 7th August 2023

DOI: 10.1039/d3ra04709a

rsc.li/rsc-advances



## Introduction

The development of cost-effective and clean energy is of considerable scientific interest due to the rapid increase in energy consumption and environmental crisis associated with fossil fuels.[1–3] Electrochemical water splitting is one of the promising strategies, which involves the hydrogen evolution reaction (HER) and oxygen evolution reaction (OER).[4] However, the commercialization of these devices is largely limited due to the high over-potential and sluggish kinetics of the OER, which requires highly active electrocatalysts.[5] Henceforth, in the last few decades, many research groups have been conducting their work in this area to develop efficient electrocatalysts for OER. Initially, precious metals (Pt, Ir and Ru) based catalysts were focused due to their robust nature and high activity.[6–10] In the recent past, the demand for cost-effective earth-abundant transition metal based electrocatalysts has accelerated to overcome the high cost and lower abundance of precious metals.[11–14] However, the OER activity of these transition metal-based catalysts has not been comparable to the Pt-group metals. Hence, the foremost challenge for chemists is to design and develop novel cost-effective, earth abundant and highly efficient catalysts as well as strategies to boost their activity for OER.

Cobalt-based catalysts have been significantly studied to facilitate the OER.[15,16] For instance, cobalt oxides,[17–20] hydroxides,[21,22] sulfides,[23–25] selenides,[26,27] phosphates/phosphides,[28,29] and nitrides[30,31] have been established as advanced electrocatalyst for OER. Beside these materials, several molecular cobalt complexes have also been found as efficient electrocatalyst for OER in recent times.[32–38] D. G. Nocera's group reported a β-octafluoro Co(III) xanthene hangman corrole as the effective OER catalyst under operating conditions at

[a]*Catalysis and Bioinorganic Research Lab, Department of Chemistry, Deshbandhu College, University of Delhi, New Delhi-110019, India. E-mail: ukumar@db.du.ac.in*
[b]*Department of Chemistry, University of Delhi, New Delhi-110007, India*
[c]*Department of Chemistry, Indian Institute of Technology, New Delhi-110016, India. E-mail: ppingole@chemistry.iitd.ac.in*
[d]*Department of Applied Chemistry, Delhi Technological University, New Delhi-110042, India*

† Electronic supplementary information (ESI) available: Crystallographic data for the complex **1** CCDC 2204239. For ESI and crystallographic data in CIF or other electronic format see DOI: https://doi.org/10.1039/d3ra04709a

‡ Deepika Tanwar and Priya Jain contributed equally to this work.

modest overpotential.[32] J. T. Groves *et al.* reported a cationic cobalt–porphyrin complex as an efficient homogeneous electrocatalyst for water oxidation to study the role of buffer on the reactivity.[33] C. N. Verani *et al.* designed a novel phenolate rich cobalt(III) complex which acts as an excellent water oxidation catalyst at moderate overpotential of 0.5 V.[34] L. Sun *et al.* used cobalt porphyrin complexes as OER catalysts and found that the *in situ* generation of cobalt oxides thin film acts as a real catalyst.[35] Recently, M. Nath *et al.* reported a cobalt complex bearing selelno-based ligand as OER electrocatalyst with very low overpotential of 320 mV.[37] Zhen-Tao Yu *et al.* reported a cobalt(IV) diacetato complex bearing a substituted bipyridine dianionic ligand as highly active electrocatalyst for OER at an overpotential of only 360 mV at pH = 6.[38] In case of molecular cobalt catalyst, many research groups reported that the *in situ* formation of $Co(OH)_2$/cobalt oxide are the true catalyst.[19,35,39]

However, the nature of *in situ* generated catalyst depends upon the molecular nature of parent catalyst and hence the efficacy of the catalyst solely depends on role of parent complex. Overall, these representative examples of Co-complex based OER catalysts highlights the chemistry of ligands towards controlling the electron-density around the Co-metal center or an ability to partially oxidize the complex to make thin films of cobalt oxide. Hence, it was thought that the Lewis base ligand can control the electron-density around metal center to enhance their catalytic activity. Further, the coordination of Lewis base and acetate moiety will provide more coordination flexibility around metal center which supports the substrate coordination/removal during catalysis to facilitate the reaction cycle.[38,40] In this view, we report a novel cost-effective lutidine coordinated cobalt(II) acetate complex $[(3,5\text{-lutidine})_2Co(OAc)_2(H_2O)_2]$ (**1**) as promising electrocatalytic activator for OER. The obtained data after OER electrocatalytic analysis indicates that complex **1** is better performer than the state-of-the-art $IrO_2$ catalyst.

# Experimental

### Materials and methods

The details of materials and methods have been given in ESI.† The details of X-ray diffraction data collection and crystallographic information are also given in the ESI (see Table S1†).

### Synthesis of complex 1

$Co(OAc)_2 \cdot 4H_2O$ (250 mg, 1 mmol) was dissolved in acetonitrile to get homogeneous solution, to which 3,5-lutidine (214 mg, 2 mmol in 5 mL acetonitrile) was added dropwise and stirred at room temperature for 3 h. The resulting solution was reduced using rotary evaporator and then kept at room temperature for crystallization. Crystals suitable for single crystal X-ray diffraction data of $[(3,5\text{-lutidine})_2Co(OAc)_2(H_2O)_2]$ (**1**) were obtained after five days. Yield: 94% (0.402 g, 0.940 mmol). FT-IR (KBr, $\nu$ in $cm^{-1}$): 3425 (br) for $\nu(H_2O)$; 1572 (s) for $\nu_{asym}(OCO)$; and 1419 (s) for $\nu_{sym}(OCO)$. Anal. calcd (%) for $C_{18}H_{28}CoN_2O_6$: C, 50.59; H, 6.60; N, 6.56. Found C, 51.02; H, 6.57; N, 6.71.

### Electrochemical analysis

The electrochemical analysis for oxygen evolution reaction was performed in a three-electrode electrochemical setup, using Glassy carbon (GC) electrode with geometric area of 0.07 $cm^2$ as working electrode, Hg/HgO (1 M NaOH) ($E^0 = 0.118$ V *vs.* RHE) as reference electrode and graphite rod as counter electrode in 1 M KOH (pH = 14). The GC electrode was modified with catalyst ink prepared by dispersing the catalyst in 3 : 1 100 μL isopropanol and water mixture using ultrasonicator. Carbon black acetylene was added as an additive in the catalyst to separate the catalyst layer with the ratio of catalyst to carbon black was 8 : 2. The loading of the catalyst on the GC surface was about 0.05 mg, which corresponds to normalized loading of 0.714 mg $cm^{-2}$. Similarly, $IrO_2$ obtained from Sigma Aldrich was also used to modify the electrode using same procedure for comparative study. All the potentials were converted to reversible hydrogen electrode (RHE) by using the following eqn (1):[41]

$$E_{RHE} = E_{Hg/HgO/OH^-} + 0.118 + (0.059\ pH) \quad (1)$$

The electrochemical measurements were performed on MetrohmAutolab 204 N instrument. The current density was normalized according to geometric surface area and electrochemical surface area. The overpotential ($\eta$) was calculated by subtracting the standard potential of water oxidation (1.23 V *vs.* RHE) from the experimental potential observed. The Double layer capacitance ($C_{dl}$) calculated from the slope of the plot of current density *vs.* scan rate, was used to estimate the electrochemically active surface area (ECSA) using eqn (2).

$$ECSA = C_{dl}/C_s \quad (2)$$

where $C_s$, is the specific capacitance of the atomically smooth surface of the material and is taken to be 0.04 mF $cm^{-2}$.[42]

The Tafel slope was calculated by using the eqn (3):

$$\eta = b \log j + a \quad (3)$$

where $\eta$ is the overpotential and $b$ is the Tafel slope. The electrochemical impedance spectroscopy (EIS) measurements were performed by applying AC potential with 10 mV amplitude in a frequency range of 0.1 Hz to $10^5$ Hz at 1.62 V *vs.* RHE. The catalyst stability was analyzed by drop casting the catalyst material on glassy carbon plate electrode in 1 M KOH for 14 hours at a constant potential 1.65 V *vs.* RHE. After the electrochemical stability, the spent catalyst material was used for post catalytic characterizations *i.e.*, FTIR, Raman, SEM, EDX and XPS.

### Calculation of TOF

The values of TOF were evaluated by assuming all the metal ions as the active catalytic centers as per the following eqn (4).[43]

$$TOF = J \times A/4 \times F \times n \quad (4)$$

Here, $J$, $A$, $F$ and $n$ are the observed current density, geometrical surface area of the working electrode (0.07 $cm^2$), Faraday

constant (96 485 C $mol^{-1}$) and number of moles of active sites present in the catalyst. Since four electrons are needed to evolve one mole of $O_2$, so the term $\frac{1}{4}$ is used. Further, $n$ was determined by dividing the mass of material loaded (0.05 mg) onto the electrode surface to the molecular mass of the sample (eqn (5)).

$$n = m/M \quad (5)$$

$$n = \frac{0.05 \times 10^{-3}\ \text{g}}{413\ \text{g mol}^{-1}} = 1.21 \times 10^{-7}\ \text{moles}$$

## Results and discussions

### Synthesis

The schematic diagram for synthetic details of complex **1** is given in Scheme 1. The reactions of $Co(OAc)_2 \cdot 4H_2O$ with 3,5-lutidine in 1 : 2 ratio in acetonitrile at room temperature afforded complex **1** in quantitative yields. IR spectra of complex **1** (Fig. SI-3a in ESI†), shows bands at 1572 (s) and 1419 (s) for $\nu_{asym}$(OCO) and $\nu_{sym}$(OCO) characteristic for monodentate acetate moieties. The broad band at 3425 $cm^{-1}$ confirms the presence of coordinated water molecules. Further, the bands at $\rho r(H_2O)$ (710 $cm^{-1}$) and $\rho w(H_2O)$ (649 $cm^{-1}$) also support the presence of coordinated water molecules.[44]

### Crystal structure

The molecular structure of complex **1** was determined by single-crystal X-ray diffraction data. The molecular structure of complex **1** with the atom labeling scheme is shown in Fig. 1. Complex **1** consists of a Co(II) atom coordinated by two 3,5-lutidine, two water molecules and two acetate moieties in monodentate mode to afford an octahedral geometry. The $Co1–O1_{water}$, $Co1–O2_{acetate}$ and $Co1–N1_{lutidine}$ distances in complex **1** are 2.131(1), 2.068(1) and 2.153(2) Å, respectively.

Significant hydrogen-bond parameters observed in complex **1** are listed in Table 1. The oxygen atom (O1) of water molecules in **1** act as hydrogen-bond donor, one to the carbonyl oxygen (O3) of the monodentate acetate within the molecule (intramolecular hydrogen bonding) and another with the carbonyl oxygen (O3) of the monodentate acetate of adjacent molecule

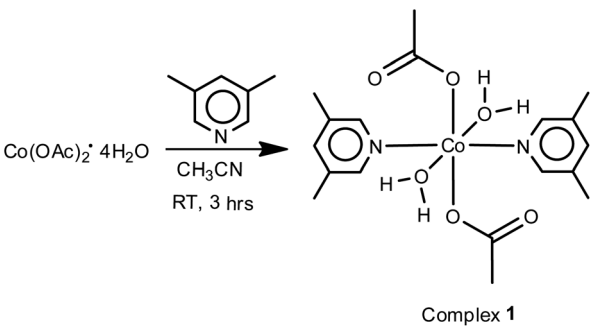


Scheme 1 Synthesis scheme of complex **1**.

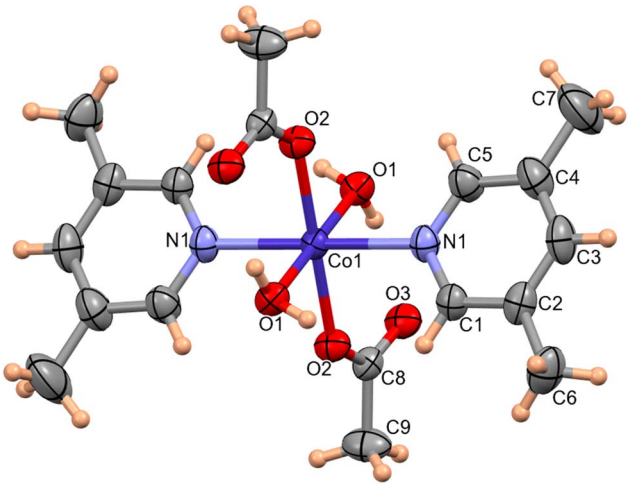


Fig. 1 ORTEP of complex **1** with 50% probability ellipsoid. Selected bond lengths (Å) and angles (°): Co1–O1 2.133(1), Co1–O2 2.068(1), Co1–N1 2.153(2); O1–Co1–O1 180.00(0), O2–Co1–O2 180.00(6), O2–Co1–N1–90.58(5), N1–Co1–N1 180.00(8), O2–Co1–O1 88.55(4), N1–Co1–O1 87.42(5).

(intermolecular hydrogen bonding) as depicted in Fig. 2a. The aforementioned hydrogen-bonding network grows to afford a three-dimensional supramolecular packing along the *c*-axis, as depicted in Fig. 2b. From packing diagram of complex **1**, it was also observed that the crystal structure has various hexagonal vacant pores formed by the supramolecular assembly which could be useful for enhancing their catalytic, separation and gas storage properties. The void volume has also been calculated to be 114 $Å^3$ per unit cell. Although the structural analysis shows a solvent accessible void volume of around 194 $Å^3$ per unit cell, it is not apparent that water molecules can enter this void and the residual density value (0.7 Å) also do not imply the presence of water molecules inside this channel. The porous nature of complex **1** is also clearly visualized in FESEM image as depicted in Fig. SI-1 in ESI.†

### Computational studies

**Frontier molecular orbitals.** The optimized geometry of complex **1** is depicted in Fig. SI-2.† The HOMO (highest occupied molecular orbital) and LUMO (lowest unoccupied molecular orbital) along with HOMO−1 and LUMO+1 have been computed through DFT using GaussView 5.0 software. Generally, the electron donating orbital is regarded as HOMO and electron accepting is LUMO. These two orbitals are most interacting in the complex, and thus called frontier orbitals.[45–48] The energy gaps were computed at LANL2DZ basis set. In

Table 1 Significant hydrogen bond distances (Å) and bond angles (°) in the crystal structure of complex **1**

| D–H···A | D–H | H···A | D···A | ∠D–H···A |
|---|---|---|---|---|
| O1–H1A···O3 | 0.860 | 1.946 | 2.708(2) | 148.70 |
| O1–H1B···O3 | 0.861 | 2.080 | 2.823(2) | 148.84 |

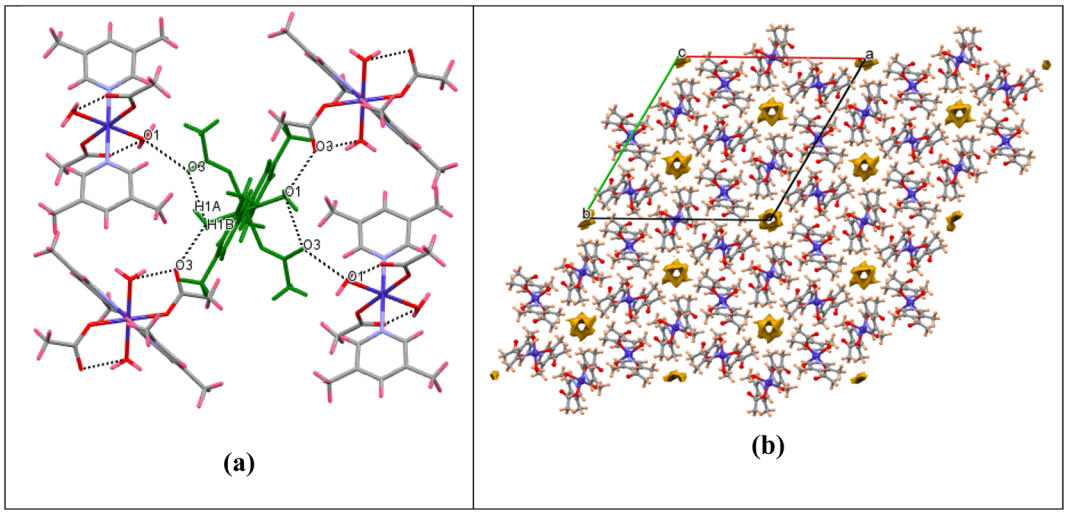


Fig. 2 (a) Packing diagram showing O–H···O hydrogen bonding for complex **1**. (b) Packing diagram showing the void surfaces in the crystal structure of complex **1**, viewed down crystallographic *c*-axis.

complex **1**, the HOMO and LUMO energies are −5.19 and −1.27 eV, respectively, leading to an energy gap of 3.92 eV (Fig. 3). Determining the energy gap is important because it displays the charge transfer behavior in a system,[49] and the chemical reactivity and stability of the molecule as a whole depends largely on the energy gap. Larger the HOMO–LUMO energy gap, greater the stability and lower is the chemical reactivity of the molecule and *vice versa*.[50,51] From the frontier molecular orbital (FMO) diagram, it has been observed that the electron density is densely accumulated around the metal ion and oxygen atoms in HOMO, while it is dispersed on and around the pyridine rings in LUMO. A slightly more gathered electronic density at the metal center is observed in HOMO−1. Thus, it is believed that the metal center is behaving as an active site for the incoming substrate to get adsorbed/attached. The subsequent steps for OER mechanism are expected to proceed from here.

**Molecular electrostatic potential surfaces.** The molecular electrostatic potential (MEP) maps provide information about the relative polarity of a particular system. The MEP of complex **1** (Fig. 4) has been computed through DFT mode, using B3LYP level of theory and LANL2DZ as basis set. The scale having different colors here indicates varied electrostatic potentials within a molecular system.[52] The order of potentials from low to high goes as red < orange < yellow < green < blue. On one end of the scale, the blue color suggests the presence of electropositive potential, while on the other end, the red color indicates the electronegative potentials, and the green color specifies zero potential. In this way, we can understand the relative polarity of a particular system.[53,54] In the present case, we observe a deep red color at the oxygen centers of acetate ligand while a positive potential around the substituted pyridine ring. Lone pair of electrons is generally associated with a negative potential; thus, a reddish coloration is observed around the oxygen centers. In addition to this, the yellowish coloration around the metal

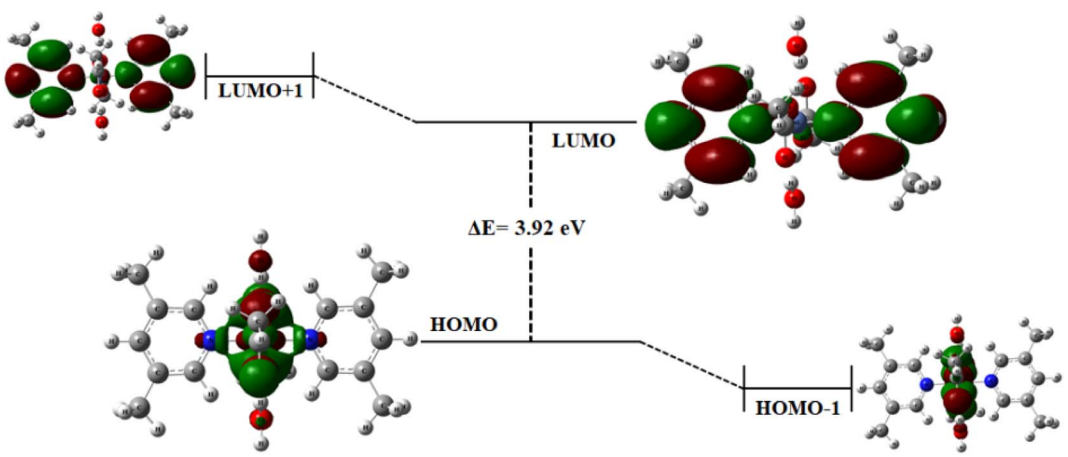


Fig. 3 Frontier molecular orbital diagram for complex **1** at iso-surface value = 0.02.

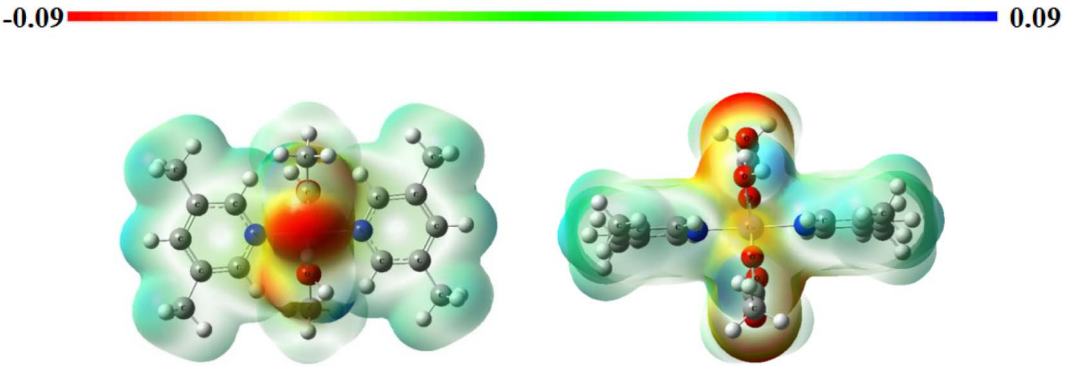


Fig. 4 Molecular electrostatic potential maps for complex **1** (iso-surface value = 0.002).

center depicts the presence of electron density in this region. These observations can be well correlated with that of FMOs, as discussed above.

**Non-covalent interactions.** The reduced gradient of density (RDG) plots reveals information about weak, intramolecular, and intermolecular interactions.[55,56] E. R. Johnson first introduced the RDG function, which is density and its first derivative together, representing the divergence from homogeneous electronic distribution.[57] It is a dimensionless quantity. Based on the reduced density gradient, $s$ and electron density, $\rho$, the NCI index plots are drawn as per eqn (6)

$$s = 1/(2(3\pi^2)^{1/3}) \times |\nabla\rho|/\rho^{4/3} \quad (6)$$

The kind of interactions existing within a molecule is further understood by the Laplacian of density, $\nabla^2\rho$, which is the sum of three eigenvectors $\lambda_1$, $\lambda_2$ and $\lambda_3$. In a certain system, $\lambda_3$ differs along the internuclear direction, whereas the other two components (*viz.* $\lambda_1$ and $\lambda_2$) describe the variation of density in the plane normal to that of $\lambda_3$ eigenvector. The value of eigenvector $\lambda_2$ mainly suggests the type of interaction present in a system. For bonding interactions, such as H-bond, the value of $\lambda_2 < 0$, while for non-bonding interactions $\lambda_2$ is greater than zero. The value of $\lambda_2$ is nearly zero for weak van der Waals interactions.[57,58] The colors in RDG plot also suggest these interactions visually. For example, the blue color stands for H-bonds, green color suggests the presence of weak van der Waals interactions and the red color depicts the steric effect.[54] Fig. 5 represents the non-covalent interactions in complex **1** and their two-dimensional RDG plots. In complex **1**, the RDG plot displays the presence of H-bonds and steric repulsions co-existing within the complex.

## Oxygen evolution activity in alkaline electrolyte

The electrocatalytic activity of the as prepared complex **1** was evaluated using Linear Sweep voltammetry (LSV) at scan rate 10 mV $s^{-1}$ in 1 M KOH solution. The complex **1** showed onset potential of 1.50 V *vs.* RHE and high current density of 100 mA $cm^{-2}$ at 1.87 V *vs.* RHE. The observed results towards OER electrocatalysis are even better than the state-of-the-art $IrO_2$ catalyst which showed OER onset potential of 1.52 V *i.e.*, 20 mV higher than complex **1**. The comparative LSV is shown in Fig. 6a. The kinetics of the catalysis towards OER of the complex **1** was also compared to that of $IrO_2$ catalyst using corresponding Tafel slope values. The commercial $IrO_2$ exhibited a slope value of 64.6 mV $dec^{-1}$, whereas the complex **1** showed 47.7 mV $dec^{-1}$. Tafel slope indicating that our catalyst is showing facile kinetics towards OER, higher than commercial $IrO_2$ catalyst (Fig. 6b). The complex **1** showed an overpotential of 530 mV to reach 40 mA $cm^{-2}$ which is 70 mV lower than that of $IrO_2$ (Fig. 6c). The comparison with similar materials in literature

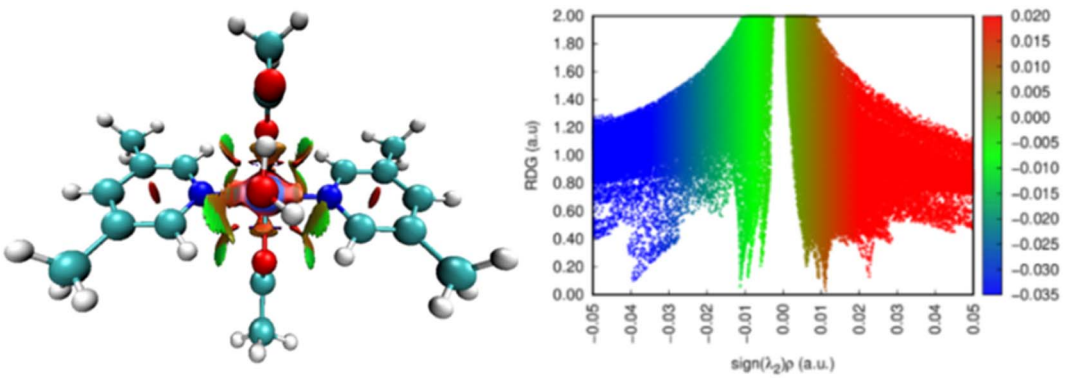


Fig. 5 Non-covalent interactions and RDG plots for complex **1** (iso-surface value = 0.5).

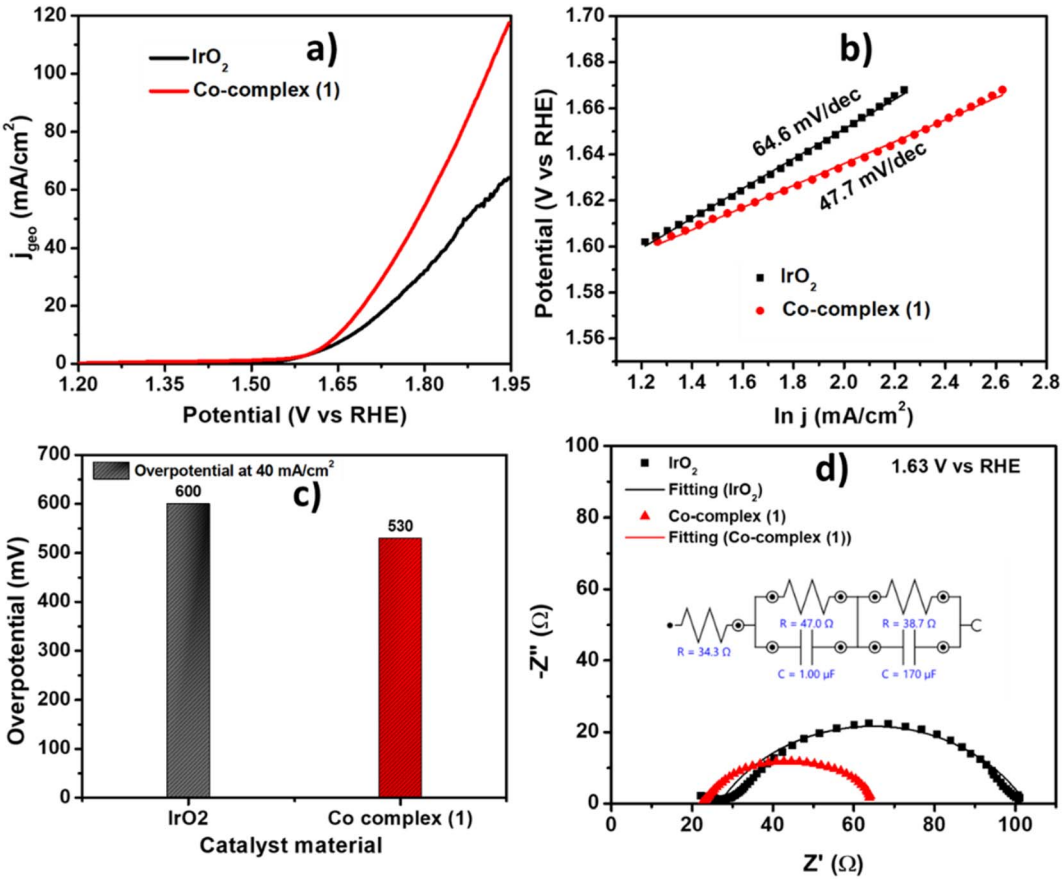


Fig. 6 (a) Comparison of LSV polarization curve for complex **1** and $IrO_2$ at 10 mV $s^{-1}$ in 1 M KOH, (b) the corresponding Tafel plots, (c) the overpotential comparison at 40 mA $cm^{-2}$ and (d) the Nyquist plot comparison for complex **1** and $IrO_2$.

was also shown in Table 2 indicating the appreciable activity of our catalyst towards OER.[34,36–38,59–61] The electrochemical impedance spectroscopy (EIS) was performed at a potential of 1.63 V *vs.* RHE to determine the charge transfer parameter for complex **1**. The diameter of the Nyquist plot is related to the charge transfer resistance at the electrode–electrolyte interface. Nyquist plots shown in Fig. 6d, showed that the complex **1** has low charge transfer resistance of 43.5 Ω, also lower than $IrO_2$ showing $R_{ct}$ of 63.8 Ω which is also consistent with the lower overpotentials required to reach higher current density from the LSV and Tafel analysis.

The $C_{dl}$ was calculated by performing CV at different scan rates (Fig. 7a and b) and plotting the current density *vs.* scan rate (Fig. 7c) which was found to be 81.3 μF and 75.8 μF for complex **1** and $IrO_2$ complex respectively. The current density normalized with ECSA was also shown in Fig. 7d, indicating the good electrocatalytic activity of Co-complex **1** in terms of high

Table 2 Comparison of the efficacy molecular cobalt electrocatalyst for OER

| Cobalt complexes | Electrolyte | Overpotential (mV)/current density (mA $cm^{-2}$) | Tafel slope (mV $dec^{-1}$) | TOF | Ref. |
|---|---|---|---|---|---|
| $[(Lut)_2Co(OAc)_2(H_2O)_2]$ | 1 M KOH | 410 ± 20/10.0 | 45.7 | 0.05 $s^{-1}$ | This work |
| $[Co(LN_2O_3)H_2O]$ | Sodium borate (pH = 11) | 500 | — | — | 34 |
| $[(L_{monoanionic})_2Co(CH_3OH)_4]^a$ | Phosphate buffer (pH = 9) | 520/0.5 | — | 5 $s^{-1}$ | 36 |
| $[Co\{(SeP^iPr_2)_2N\}_2$ | 1 M KOH | 320/10.0 | 61.6 | 0.032 $s^{-1}$ | 37 |
| $[Co(bipyalk)(OAc)_2]^a$ | Phosphate buffer (pH = 6) | 360/1.0 | — | 1.5 $s^{-1}$ | 38 |
| $[Co@CB[5]]^a$/ITO | Borate buffer (pH = 9.2) | 485/1.0 | 59.5 | 0.3 $s^{-1}$ | 59 |
| $[Co^{II}Co^{III}(\mu\text{-}OAc)(\mu_3\text{-}OH)(\mu\text{-}L_{trianionic})]_2^a$ | Sodium phosphate buffer of pH 7 | 768/1.0 | 320 | 1.1 × $10^{-3}$ $h^{-1}$ | 60 |
| $[CoL_{dianionic}]^a$ | Buffer pH-11 | 360/10.0 | 135.9 | — | 61 |

[a] $L_{monoanionic}$ = (*E*)-4-((2-hydroxynaphthalen-1-yl)diazenyl)benzenesulfonate), bipyalk = 2,2′-([2,2′-bipyridine]-6,6′-diyl)bis(propan-2-ol), CB[5] = cucurbit[5]uril, $L_{trianionic}$ = *N*′,*N*″-(5-methyl-2-oxido-1,3-phenylene)bis(methan-1-yl-1-ylidene)bis(4-methoxybenzoylhydrazonate), $L_{dianionic}$ = 4-chloro-1,2-bis[2-hydroxy-5-(phenylazo)benzylideneamino]benzene).

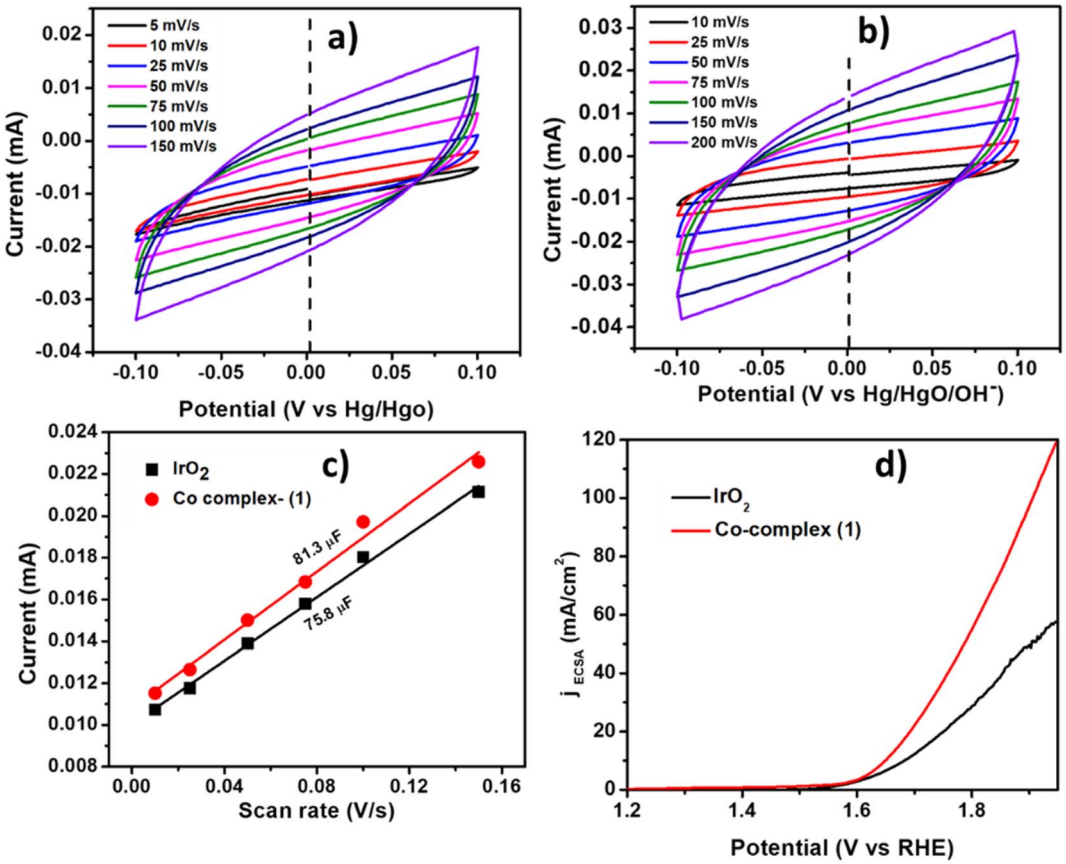


Fig. 7 The CVs (cyclic voltammograms) at different scan rates in the capacitive region for (a) $IrO_2$ and (b) complex **1**, (c) the plot of current *vs.* scan rates for $C_{dl}$ calculation, (d) the comparison of LSV curves normalized by ECSA for complex **1** and $IrO_2$.

current density towards electrocatalytic OER. The summary of the OER electrochemical parameters is shown in Table 3.

The turn over frequency, which indicates the intrinsic activity of the catalyst was calculated by using the equation given in the experimental section. The complex **1** showed the two times higher TOF ($0.05\ s^{-1}$) at 1.73 V as compared to $IrO_2$ ($0.02\ s^{-1}$) (Fig. 8a). The long term stability of complex **1** was also checked using chronoamperometry method, by applying a constant potential of 1.65 V for 14 hours. It was observed (Fig. 8b) that the catalyst showed high stability with retention of 95% current. The CV curves before and after the OER stability are given in the inset of Fig. 8b, showing a slight decrement in

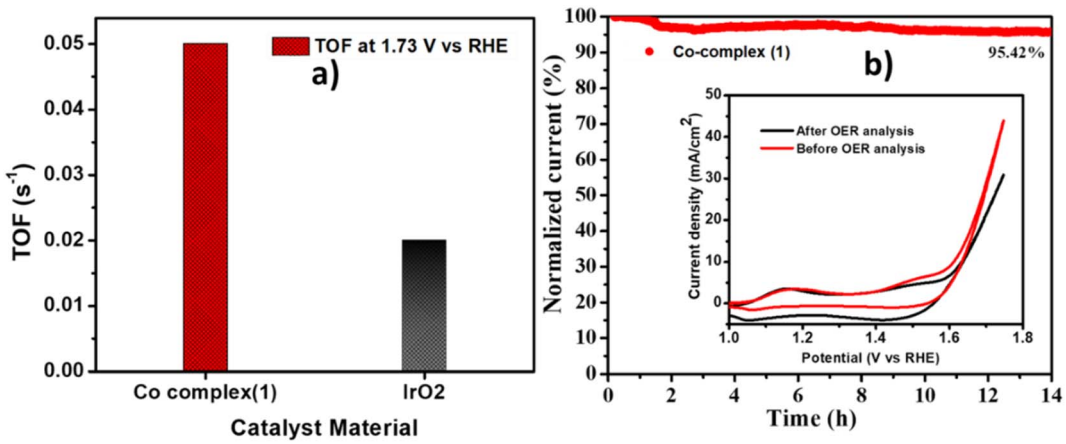


Fig. 8 (a) The comparison of TOF at 1.73 V *vs.* RHE for Co-complex (**1**) and $IrO_2$, (b) chronoamperometry curve at 1.65 V *vs.* RHE for 14 hours for Co-complex (**1**).

Table 3 The comparison of activity parameters for OER for Co-complex (**1**) and $IrO_2$

| Parameters | Complex **1** | $IrO_2$ |
|---|---|---|
| $E_{onset}$ (V *vs.* RHE) | 1.51 ± 0.01 | 1.52 |
| $\eta_{10mA/cm^2}$ (mV *vs.* RHE) | 410 ± 20 | 440 |
| Tafel slope (mV $dec^{-1}$) | 45.7 | 64.6 |
| Mass activity (mA $mg^{-1}$) @ 1.64 | 14 | 8.5 |
| $R_{ct}$ (Ω) | 43.5 | 63.8 |
| $C_{dl}$ (μF) | 81.3 | 78.5 |
| TOF (1.73 V *vs.* RHE) | 0.05 | 0.02 |
| $\alpha$ | 0.59 | 0.56 |

the current density after 14 hours of stability, indicating robustness of the catalyst.

The post catalytic characterisation of the spent electrodes (after OER analysis) were performed after the durability test on the Co-complex (**1**). The post catalytic FTIR (Fig. SI-3a in ESI†) shows the peak at 3431 $cm^{-1}$ corresponding to the –OH vibration, 2921 $cm^{-1}$ for Co–OH stretching. The peak present at 1633 $cm^{-1}$ corresponds to Co–O.[62,63] These peaks in the post OER FTIR suggests that the formation of $Co(OH)_2$/CoOOH could act as the main active sites for the OER. However, along with these, some peaks matching with the initial spectra at 1038 and 1153 $cm^{-1}$ indicate that the complex **1** is not totally degraded/decomposed after catalysis. The spectra suggests that the oxidation of Co(II) to Co(III) occurs at high oxidation potential and Co act as the catalytic centre for OER. The FESEM image after catalysis shows agglomeration of the particles (Fig. SI-3b in ESI†). The EDX spectra as shown in Fig. SI-4a in ESI†) indicates the presence of C, N, Co and O in the Co-complex (**1**). After catalysis (Fig. SI-4b in ESI†), the EDX of the sample displays an increase in the O content as well as presence of Co, C, N and K (due to KOH as electrolyte) indicating the presence of $Co(OH)_2$ at the surface of the catalyst. The elemental mapping (Fig. SI-5 in ESI†) shows the uniform distribution of the elements on the surface before and after catalysis which indicates that the complex is not totally changed to hydroxide species. This suggests that formation of thin layer of $Co(OH)_2$/CoOOH can be the reason for high activity of Co-complex (**1**) towards OER.

The X-ray photoelectron spectroscopy was performed to further understand the chemical composition and oxidation state in the pre and post catalytic OER samples as shown in Fig. 9. The Co 2p core level spectra of Co-complex (**1**) (Fig. 9a) shows two peak at 780.85 eV ($Co^{2+}$ $2p_{3/2}$) and 796.49 eV ($Co^{2+}$ $2p_{1/2}$) and two strong satellite peaks confirming the presence of $Co^{2+}$ in the sample. After OER analysis, the slight shift of the $Co^{2+}$ peak to 780.19 eV and the appearance of $Co^{3+}$ peak at 782.18 eV is in accordance with the FTIR analysis, confirming that the formation of $Co(OH)_2$ and CoOOH at the surface.[64] The M–O and M–OH peak intensity increases in the post catalytic O 1s spectra (Fig. 9b) also showing the formation of $Co(OH)_2$ at the surface. The C 1s XPS spectra shows the presence of C–C

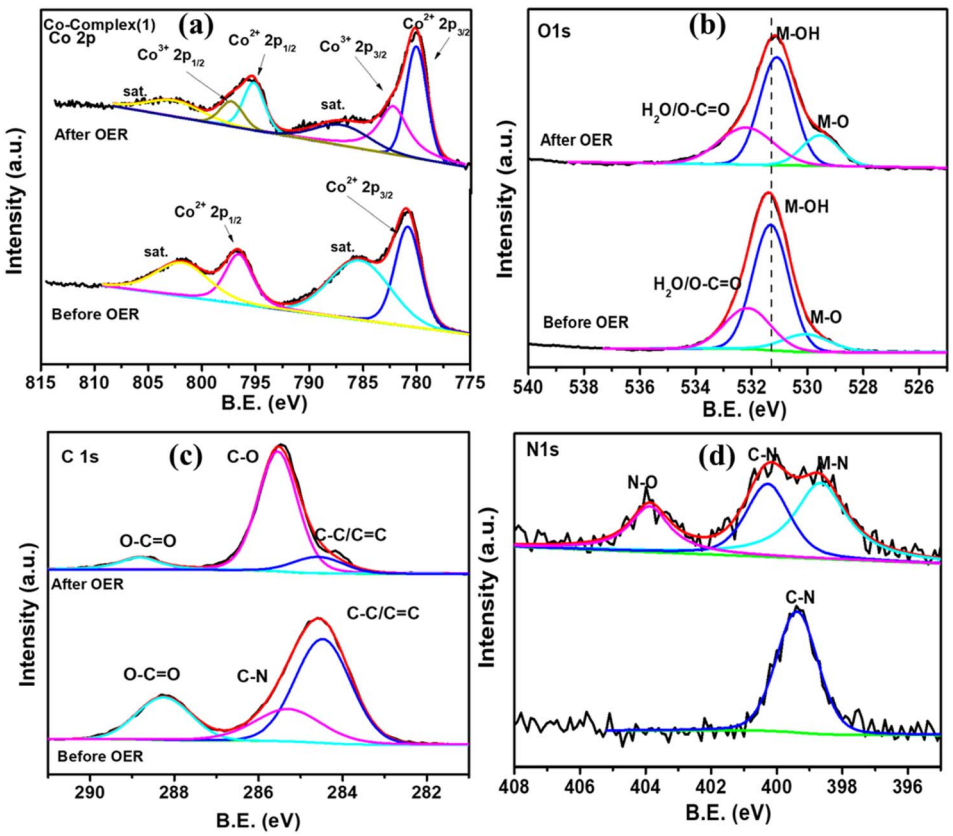


Fig. 9 XPS core level spectra comparison of (a) Co 2p, (b) O 1s, (c) C 1s and (d) N 1s before and after catalysis of Co-complex (**1**).

(284.6), C–N (285.4) and O–C=O (288.2) in the pristine sample. After catalysis, the relative composition of C–C decreases and C–O increases. This indicates the oxidation of C due to the oxidative environment provided by OER. Similarly the occurance of N–O peak in N 1s spectra is also due to oxidation. Thus, the post catalytic XPS, FTIR and EDX analysis confirmed the retention of the electrocatalyst in terms of bulk composition, and formation of $Co^{2+}$ ($Co(OH)_2$) and $Co^{3+}$ (CoOOH) plays a crucial role during OER.

The high OER performance of the Co-complex (**1**) may have been resulted due to its highly porous connected network, high accessible Co active centres and high surface area. The interconnected network arising from the OH···O hydrogen bonding leads to a 3-D structure with hexagonal vacant pores which helped inenhancing mass transfer and ion transport at the electrode–electrolyte interface leading to high electrocatalytic performance of the Co-complex **1**.

## Conclusion

We have the novel lutidine coordinated cobalt(II) acetate complex $[(3,5\text{-lutidine})_2Co(OAc)_2(H_2O)_2]$ (**1**) by simplest condensation reaction. The structure of complex **1** was determined by single crystal X-ray diffraction data and found distorted octahedral geometry around the metal center. The noncovalent interaction found in complex **1** resulted in O–H···O hydrogen-bonding network that grown in a three-dimensional structure with various hexagonal vacant pore which could be useful for enhancing their catalytic activity. The comparative study of geometrical parameters obtained from the XRD data and DFT calculations was found in good agreement. The MEP maps analysis depicted the electron rich centers in the complex **1** are also found well in agreement with the solid-state structure. It was thought that the coordination flexibility and electron rich centers around metal center will also support in the enhancement of their catalytic activity. The Co-complex **1** showed excellent electrocatalytic OER activity better than state-of-the-art $IrO_2$, which may be due to the 3D porous structure, rapid transport of ions and high accessible Co active sites, higher electron density, and coordination flexibility around metal center. Further, the post catalytic XPS, FTIR and EDX analysis also confirmed the retention of the electrocatalyst in terms of bulk composition, and formation of $Co^{2+}$ ($Co(OH)_2$) and $Co^{3+}$ (CoOOH) OER.

## Data availability

All data generated or analyzed during this study are included in this published article and its ESI.†.

## Author contributions

DT: investigation, writing, PJ: electrochemical study and writing, DA: computational studies, Athul Sudheendranath and Sajesh P. Thomas: SCXRD, UK: supervision, writing, review & editing, PPI: supervision, writing, review & editing.

## Conflicts of interest

The authors declare that they have no conflicts of interest.

## Acknowledgements

The authors UK and PPI acknowledge the Science and Engineering Board (SERB) New Delhi, India for funding [TAR/2020/000232]. DT and PJ acknowledge University Grant Commission and IIT Delhi for research fellowship. Authors also acknowledge the Department of Chemistry and University Science Instrumentation Center, University of Delhi, and Department of Chemistry, IIT Delhi for instrumental facilities.

## References

1 T. Yao, X. An, H. Han, J. Q. Chen and C. Li, *Adv. Energy Mater.*, 2018, **8**, 1800210.
2 D. Fa, J. Yuan, G. Feng, S. Lei and W. Hu, *Angew. Chem., Int. Ed.*, 2023, **62**, e202300532.
3 Y. Qiu, Z. Liu, X. Zhang, A. Sun and J. Liu, *J. Colloid Interface Sci.*, 2022, **625**, 50–58.
4 Y. Chen, M. Wang, S. Xiang, J. Liu, S. Feng, C. Wang, N. Zhang, T. Feng, M. Yang, K. Zhang and B. Yang, *ACS Sustainable Chem. Eng.*, 2019, **7**, 10912–10919.
5 T. Ghosh and G. Maayan, *Angew. Chem., Int. Ed.*, 2019, **58**, 2785–2790.
6 S. W. Gersten, G. J. Samuels and T. J. Meyer, *J. Am. Chem. Soc.*, 1982, **104**, 4029–4030.
7 T. Reier, M. Oezaslan and P. Strasser, *ACS Catal.*, 2012, **2**, 1765–1772.
8 L. C. Seitz, C. F. Dickens, K. Nishio, Y. Hikita, J. Montoya, A. Doyle, C. Kirk, A. Vojvodic, H. Y. Hwang, J. K. Norskov and T. F. Jaramillo, *Science*, 2016, **353**, 1011–1014.
9 Q. Shi, C. Zhu, D. Duand and Y. Lin, *Chem. Soc. Rev.*, 2019, **48**, 3181–3192.
10 B. Deng, Y. Long, C. Yang, P. Du, R. Wang, K. Huang and H. Wu, *Chem. Commun.*, 2021, **57**, 7830–7833.
11 S. Anantharaj, S. R. Ede, K. Sakthikumar, K. Karthick, S. Mishra and S. Kundu, *ACS Catal.*, 2016, **6**, 8069–8097.
12 Q. Liang, J. Chen, F. Wang and Y. Li, *Coord. Chem. Rev.*, 2020, **424**, 213488.
13 J. Yu, F. A. Garcés-Pineda, J. González-Cobos, M. Peña-Díaz, C. Rogero, S. Giménez, M. C. Spadaro, J. Arbiol, S. Barja and J. R. Galán-Mascarós, *Nat. Commun.*, 2022, **13**, 4341.
14 Z. P. Wu, X. F. Lu, S. Q. Zang and X. W. Lou, *Adv. Funct. Mater.*, 2020, **30**, 1910274.
15 W. Zhang, L. Cui and J. Liu, *J. Alloys Compd.*, 2020, **821**, 153542.
16 A. Badruzzaman, A. Yuda, A. Ashok and A. Kumar, *Inorg. Chim. Acta*, 2020, **511**, 119854.
17 L. Reith, C. A. Triana, F. Pazoki, M. Amiri, M. Nyman and G. R. Patzke, *J. Am. Chem. Soc.*, 2021, **143**, 15022–15038.
18 B. Paul, P. Bhanja, S. Sharma, Y. Yamauchi, Z. A. Alothman, Z. L. Wang and R. B. A. Bhaumik, *J. Colloid Interface Sci.*, 2021, **582**, 322–332.

19 F. T. Haase, A. Bergmann, T. E. Jones, J. Timoshenko, A. Herzog, H. S. Jeon, C. Rettenmaier and B. R. Cuenya, *Nat. Energy*, 2022, **7**, 765–773.
20 Y. Zhang, Q. Fu, B. Song and P. Xu, *Acc. Mater. Res.*, 2022, **3**, 1088–1100.
21 F. Lyu, Y. Bai, Q. Wang, L. Wang, X. Zhanga and Y. Yin, *Dalton Trans.*, 2017, **46**, 10545–10548.
22 B. Zhang, J. Zhang, X. Tan, D. Tan, J. Shi, F. Zhang, L. Liu, Z. Su, B. Han, L. Zheng and J. Zhang, *Chem. Commun.*, 2018, **54**, 4045.
23 S. Y. Chae, Y. J. Hwang, J. H. Choi and O. S. Joo, *Electrochim. Acta*, 2013, **114**, 745–749.
24 S. B. Kale, A. C. Lokhande, R. B. Pujari and C. D. Lokhande, *J. Colloid Interface Sci.*, 2018, **532**, 491–499.
25 Y. Kang, Y. He, D. Pohl, B. Rellinghaus, D. Chen, M. Schmidt, V. Süß, Q. Mu, F. Li, Q. Yang, H. Chen, Y. Ma, G. Auffermann and G. L. C. Felser, *ACS Appl. Mater. Interfaces*, 2022, **14**, 19324–19331.
26 M. Liaoa, G. Zenga, T. Luoa, Z. Jina, Y. Wanga, X. Koua and D. Xiao, *Electrochim. Acta*, 2016, **194**, 59–66.
27 Q. S. Zhong, W. Y. Xia, B. C. Liu, C. W. Xu and N. Li, *Int. J. Hydrogen Energy*, 2019, **44**, 10182–10189.
28 J. Chang, Y. Xiao, M. Xiao, J. Ge, C. Liu and W. Xing, *ACS Catal.*, 2015, **5**, 6874–6878.
29 M. Zhu, Y. Zhou, Y. Sun, C. Zhu, L. Hu, J. Gao, H. Huang, Y. Liu and Z. Kang, *Dalton Trans.*, 2018, **47**, 5459–5464.
30 P. Chen, K. Xu, Y. Tong, X. Li, S. Tao, Z. Fang, W. Chu, X. Wua and C. Wu, *Inorg. Chem. Front.*, 2016, **3**, 236–242.
31 X. Peng, C. Pi, X. Zhang, S. Li, K. Huo and P. K. Chu, *Sustainable Energy Fuels*, 2019, **3**, 366.
32 D. K. Dogutan, R. McGuire Jr and D. G. Nocera, *J. Am. Chem. Soc.*, 2011, **133**, 9178–9180.
33 D. Wang and J. T. Groves, *Proc. Natl. Acad. Sci. U. S. A.*, 2013, **110**, 15579.
34 S. Gonawala, H. Baydoun, L. Wickramasinghe and C. N. Verani, *Chem. Commun.*, 2016, **52**, 8440–8443.
35 Q. Daniel, R. B. Ambre, B. Zhang, B. Philippe, H. Chen, F. Li, K. Fan, S. Ahmadi, H. Rensmo and L. Sun, *ACS Catal.*, 2017, **7**, 1143–1149.
36 H. T. Shi, X. X. Li, F. H. Wu and W. B. Yu, *Dalton Trans.*, 2017, **46**, 16321–16326.
37 I. M. Abdullahi, J. Masud, P. C. Ioannou, E. Ferentinos, P. Kyritsis and M. Nath, *Molecules*, 2021, **26**, 945.
38 Y. F. Su, W. Z. Luo, W. Q. Lin, Y. B. Su, Z. J. Li, Y. J. Yuan, J. F. Li, G. H. Chen, Z. Li, Z. T. Yu and Z. Zou, *Angew. Chem., Int. Ed.*, 2022, **61**, e202201430.
39 A. Valizadeh, R. Bikas, S. Nandy, T. Lis, K. H. Chae and M. M. Najafpour, *Dalton Trans.*, 2022, **51**, 220–230.
40 U. Kumar, J. Thomas and N. Thirupathi, *Inorg. Chem.*, 2010, **49**, 62–72.
41 P. Jain, S. Jha and P. P. Ingole, *Sustainable Energy Fuels*, 2022, **6**, 1094–1107.
42 Y. Yang, H. Fei, G. Ruan and J. M. Tour, *Adv. Mater.*, 2015, **27**, 3175–3180.
43 R. K. Tripathy, A. K. Samantaraand and J. N. Behera, *Dalton Trans.*, 2019, **48**, 10557–10564.
44 S. C. Manna, S. Mistria and A. D. Jana, *CrystEngComm*, 2012, **14**, 7415–7422.
45 C. Quintana, G. Silva, A. H. Klahn, V. Artigas, M. Fuentealba, C. Biot, I. Halloum, L. Kremer, N. Novoa and R. Arancibia, *Polyhedron*, 2017, **134**, 166–172.
46 C. Soriano-Correa, C. Barrientos-Salcedo, M. Francisco-Marquez and C. I. Sainz-Díaz, *J. Mol. Graphics Modell.*, 2018, **81**, 116–124.
47 N. Elangovan, R. Thomas, S. Sowrirajan, K. P. Manoj and A. Irfan, *Polycyclic Aromat. Compd.*, 2021, **42**, 6818–6835.
48 S. M. Hiremath, A. Suvitha, N. R. Patil, C. S. Hiremath, S. S. Khemalapure, S. K. Pattanayak, V. S. Negalurmath and K. Obelannavar, *J. Mol. Struct.*, 2018, **1171**, 362–374.
49 K. Karrouchi, S. A. Brandán, Y. Sert, H. El-marzouqi, S. Radi, M. Ferbinteanu, M. E. A. Faouzi, Y. Garcia and M. Ansa, *J. Mol. Struct.*, 2020, **1219**, 128541.
50 M. Alizadeh, Z. Mirjafary and H. Saeidian, *J. Mol. Struct.*, 2020, **1203**, 127405.
51 N. Elangovan, R. Thomas and S. Sowrirajan, *J. Mol. Struct.*, 2022, **1250**, 131762.
52 M. Shahid, M. Salim, M. Khalid, M. N. Tahir, M. U. Khan and A. A. C. Braga, *J. Mol. Struct.*, 2018, **1161**, 66–75.
53 M. Thirunavukkarasu, G. Balaji, S. Muthu, B. R. Raajaraman and P. Ramesh, *Chem. Data Collect.*, 2021, **31**, 100622.
54 K. P. Manoj, N. Elangovan and S. Chandrasekar, *Inorg. Chem. Commun.*, 2022, **139**, 109324.
55 A. Prabakaran, V. Vijayakumar, N. Radhakrishnan, R. Chidambaram and S. Muthu, *Polycycl. Aromat. Compd.*, 2020, **42**, 925–941.
56 J. M. del Campo, J. L. Gázquez, R. J. Alvarez-Mendez and A. Vela, *Int. J. Quantum Chem.*, 2012, **112**, 3594–3598.
57 E. R. Johnson, S. Keinan, P. Mori-Sánchez, J. Contreras-García, A. J. Cohen and W. Yang, *J. Am. Chem. Soc.*, 2010, **132**, 6498–6506.
58 C. Lefebvre, G. Rubez, H. Khartabil, J. C. Boisson, J. C. García and E. Hénon, *Phys. Chem. Chem. Phys.*, 2017, **19**, 17928–17936.
59 F. Li, H. Yang, Q. Zhuo, D. Zhou, X. Wu, P. Zhang, Z. Yao and L. Sun, *Angew. Chem.*, 2021, **133**, 2004–2013.
60 A. K. Srivastava, A. Mondal, S. Konar and S. Pal, *Dalton Trans.*, 2022, **51**, 4510–4521.
61 Z. Shaghaghi, P. S. Kouhsangini and R. Mohammad-Rezaei, *Appl. Organomet. Chem.*, 2021, **35**, e6103.
62 A. D. Jagadale, D. P. Dubal and C. D. Lokhande, *Mater. Res. Bull.*, 2012, **47**, 672–676.
63 M. Adeel, S. Parisi, M. Mauceri, K. Asif, M. Bartoletti, F. Puglisi, I. Caligiuri, M. M. Rahman, V. Canzonieri and F. Rizzolio, *ACS Omega*, 2021, **43**, 28611–28619.
64 P. Jain, S. Jha and P. P. Ingole, *ACS Appl. Energy Mater.*, 2023, **6**, 3278–3290.